

Simulation of the electrocaloric effect based on first-principles methods

Claudio Cazorla^{1,*}

¹*School of Materials Science and Engineering, UNSW Australia, Sydney NSW 2052, Australia*

Due to critical environmental and technological issues, there is a pressing need to switch from current refrigeration methods based on compression of gases to novel solid-state cooling technologies. Solid-state cooling is based on the thermal response of materials to external magnetic, electric, or mechanic fields, the so-called caloric effect. The electrocaloric (EC) effect, which is caused by electric fields and typically occurs in polar materials, is particularly promising from a technological point of view owing to its good scalability and natural implementation in circuitry. Simulation of EC effects represents an efficient and physically insightful strategy for advancing the field of solid-state cooling by complementing, and in some cases guiding, experiments. Theoretical estimation of EC effects can be achieved with different approaches ranging from computationally inexpensive but physically insightful phenomenological free-energy models to computationally very demanding and quantitatively accurate first-principles methods. In this Chapter, we review EC simulation approaches that rely on first-principles methods. In this category, we include *ab initio* quasi-harmonic methods, bond-valence and classical interatomic potentials and effective Hamiltonians. In analogy to the experiments, these simulation approaches can be used to estimate EC effects either directly or indirectly and we review here well-established protocols that can be followed for each case. The Chapter finalises with a collection of representative examples in which first-principles based approaches have been used to predict and understand original EC effects.

CONTENTS

I. Introduction	1
II. Computational Methods	2
A. <i>Ab initio</i> methods	2
B. Bond-valence and classical interatomic potentials	4
C. Effective Hamiltonians	5
III. Indirect estimation of the EC effect	6
IV. Clausius-Clapeyron method	7
V. Direct estimation of the EC effect	8
VI. Representative examples	9
A. Multiferroic BiCoO ₃ thin films	9
B. Bulk hybrid perovskite CH ₃ NH ₃ PbI ₃	11
C. Relaxor ferroelectric BaZr _{1-x} Ti _x O ₃	14
VII. Conclusions	15
References	15

I. INTRODUCTION

Polar materials exhibit a net electric dipole, also called polarization, which can be modified by temperature or an electric field. From a crystallographic point of view, polar materials are characterized by non-centrosymmetric atomic structures that lack inversion symmetry. Oxide

perovskites like BaTiO₃ and PbTiO₃ are archetypal polar materials in which their electric polarization is strongly coupled with their structural degrees of freedom [1]. Magnetism may coexist with polar order in some of these compounds, the so-called multiferroics (e.g., BiFeO₃ and BiCoO₃ [2–4]), which may add further functionality to this class of materials [5]. Oxide perovskites can be synthesized in a wide variety of forms and sizes, like ceramics, thin films, nanocrystals and nanowires, by using well-established synthesis methods (e.g., solid-state reactions and chemical vapour and pulsed laser deposition techniques). Thus, owing to their unique functionality and morphological versatility, polar materials are found in a large number of technological applications related to the fields of information storage, electronic devices, and energy conversion [6–8].

The isothermal entropy changes associated with fluctuations in the electric, magnetic and structural properties of polar materials can be large, $|\Delta S| \sim 100 \text{ kJK}^{-1}\text{kg}^{-1}$, hence they may render sizable caloric effects (i.e., adiabatic temperature changes of $|\Delta T| \sim 10 \text{ K}$). Solid-state cooling is an environmentally friendly, highly energy-efficient, and highly scalable technology that exploits caloric effects in materials for refrigeration purposes [9–15]. By applying external fields on caloric materials it is possible to achieve reversible temperature shifts that can be integrated in cooling cycles and do not involve the use of greenhouse gases. Due to their natural implementation in circuitry, polar materials are specially well suited for solid-state cooling applications based on electrocaloric (EC) effects, which are driven by electric fields (see, for instance, works [16–20]).

The magnitude of EC effects can be estimated accurately with theoretical and atomistic simulation methods. Computer simulations can be used to rationalize the origins of experimentally observed EC phenomena

* c.cazorla@unsw.edu.au

since the materials and phase transitions of interest can be accessed at the atomic scale under controlled conditions. Moreover, from a resources point of view computer simulations are inexpensive. For instance, by using open-source software and modest computer resources one already can simulate complex EC effects and assess the magnitude of the accompanying isothermal entropy and adiabatic temperature shifts. Thus, modeling of EC effects can be done systematically in order to complement and also guide the experiments.

The reliability of computer simulations, however, depends strongly on the simplifications made on the adopted structural and interaction models. Typically, increasing the reliability of the structural model comes at the expense of reducing the accuracy in the description of the interatomic forces (due to practical limitations, see Fig.1). For instance, if the simulation approach to be employed is accurate first-principles methods the calculations are likely to be performed at zero temperature by considering perfectly ordered atomic structures. Such simulation conditions obviously differ from the actual experimental conditions. On the other hand, to simulate EC effects directly at finite temperatures for realistic systems containing crystalline defects and/or other inhomogeneities one should use classical interatomic potentials or effective Hamiltonians, which may suffer from transferability issues and in general have modest predictive power. Fortunately, there are well-established simulation approaches that allow to achieve a suitable balance between computational accuracy and model reliability, and it is responsibility of the modeler to use them adequately for obtaining meaningful results.

In this Chapter, we review computational techniques based on first-principles methods that can be used to estimate theoretically and predict EC effects. We start by briefly describing genuine first-principles methods, like density functional theory, and other practical approaches that rely on them to mimic polar materials, namely, bond-valence interatomic potentials and effective Hamiltonians. Next, the simulation strategies that are employed to assess EC effects with such methods, either directly or indirectly, are reviewed. We finalize the Chapter by providing some representative examples in which first-principles based methods have been used to discover and characterize original EC effects for multiferroic thin films [27], bulk hybrid organic-inorganic perovskites [28], and relaxor ferroelectrics [29].

II. COMPUTATIONAL METHODS

The foundations of Density Functional Theory (DFT), a first-principles approach widely used in condensed-matter and materials science, bond-valence and classical interatomic potentials and effective Hamiltonians are briefly reviewed next. The two latter computational approaches are approximate and rely on the outputs of accurate first-principles methods (also called *ab initio*),

typically DFT. The computational cost of DFT methods is several orders of magnitude higher than those of interatomic potentials and effective Hamiltonians (Fig.1), hence most of the times first-principles methods cannot be used straightforwardly to estimate EC effects.

A. *Ab initio* methods

In solids, the dynamics of the electrons and nuclei can be decoupled to a good approximation because their respective masses differ by several orders of magnitude. The wave function of the corresponding many-electron system, $\Psi(\mathbf{r}_1, \mathbf{r}_2, \dots, \mathbf{r}_N)$, therefore can be determined by solving the Schrödinger equation corresponding to the non-relativistic Born-Oppenheimer Hamiltonian:

$$H = -\frac{1}{2} \sum_i \nabla_i^2 - \sum_I \sum_i \frac{Z_I}{|\mathbf{R}_I - \mathbf{r}_i|} + \frac{1}{2} \sum_i \sum_{j \neq i} \frac{1}{|\mathbf{r}_i - \mathbf{r}_j|}, \quad (1)$$

where Z_I are the nuclear charges, \mathbf{r}_i the positions of the electrons, and \mathbf{R}_I the positions of the nuclei, which are considered fixed. In real materials, Ψ is a complex mathematical function that in most cases is unknown. At the heart of any first-principles method is to find a good approximation for Ψ , or an equivalent quantity (e.g., the electronic density), that is manageable enough to perform calculations. Examples of *ab initio* methods include density functional theory (DFT), Møller-Plesset perturbation theory (MP2), the coupled-cluster method with single, double and perturbative triple excitations [CCSD(T)], and quantum Monte Carlo (QMC), to cite just a few. Among these techniques, DFT methods are frequently applied to the study of ferroelectrics and multiferroics and for this reason we summarise their foundations in what follows.

In 1965, Kohn and Sham developed a pioneering theory to effectively calculate the energy and properties of many-electron systems without the need of explicitly knowing Ψ [30 and 31]. The main idea underlying this theory, called density functional theory (DFT), is that the exact ground-state energy, E , and electron density, $n(\mathbf{r})$, can be determined by solving an effective one-electron Schrödinger equation of the form:

$$H_{\text{KS}} \Psi_{i\sigma} = \epsilon_{i\sigma} \Psi_{i\sigma}, \quad (2)$$

where H_{KS} is the Kohn-Sham Hamiltonian, index i labels different one-electron orbitals and σ different spin states. The KS Hamiltonian can be expressed as:

$$H_{\text{KS}} = -\frac{1}{2} \nabla^2 + V_{\text{ext}}(\mathbf{r}) + \int \frac{n(\mathbf{r}')}{|\mathbf{r} - \mathbf{r}'|} d\mathbf{r}' + V_{\text{xc}}(\mathbf{r}), \quad (3)$$

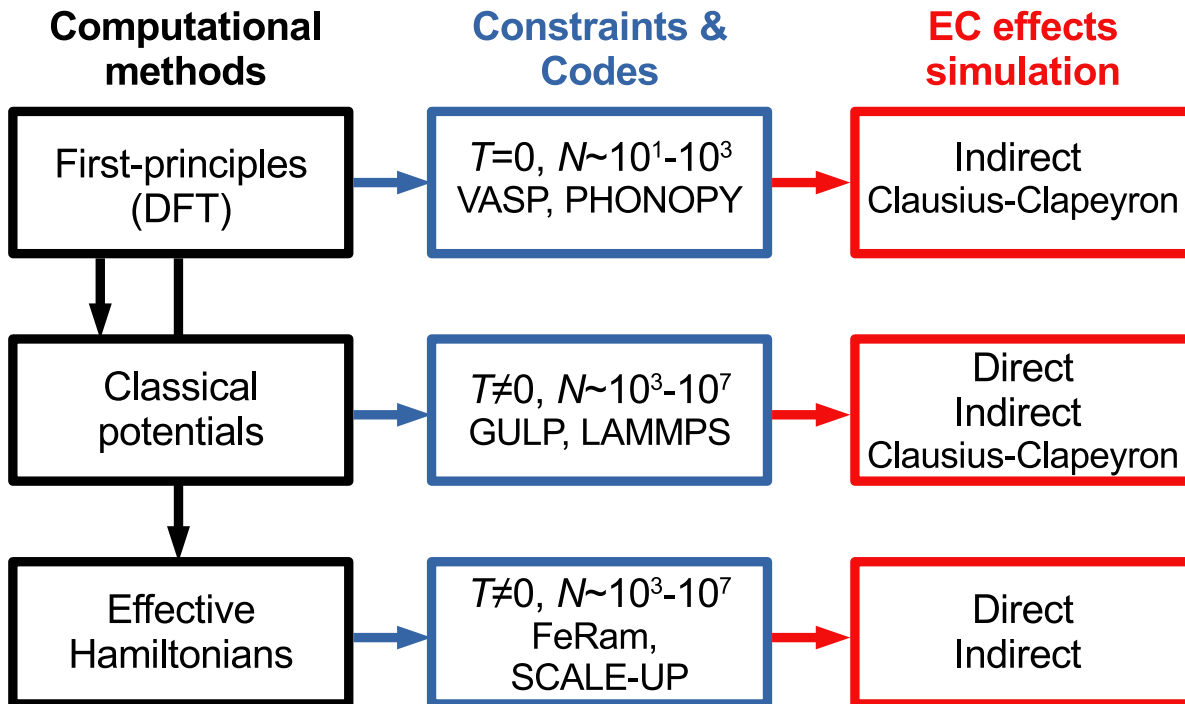


FIG. 1: Overview of computational approaches based on first-principles methods that can be used to estimate EC effects. The typical system sizes that can be simulated with them, N , along with some software codes in which they have been implemented, and the usual modalities of EC simulation that can be done with them are indicated. VASP [21], PHONOPY [22], GULP [23], LAMMPS [24], FeRam [25], and SCALE-UP [26] stand for software codes.

where

$$n(\mathbf{r}) = \sum_{i\sigma} |\Psi_{i\sigma}(\mathbf{r})|^2, \quad (4)$$

V_{ext} represents an external field and $V_{xc}(\mathbf{r}) = \delta E_{xc}/\delta n(\mathbf{r})$ is the exchange-correlation potential.

The exchange-correlation energy has a purely quantum mechanical origin and can be defined as the interaction energy difference between a quantum many-electron system and its classical counterpart. Despite E_{xc} represents a relatively small fraction of the total energy, this contribution is extremely crucial for all materials and molecules because it acts directly on the bonding between atoms. In general, $E_{xc}[n]$ is unknown and needs to be approximated. This is the only source of fundamental error in DFT methods. In standard DFT approaches $E_{xc}[n]$ is approximated with the expression:

$$E_{xc}^{\text{approx}}[n] = \int \epsilon_{xc}^{\text{approx}}(\mathbf{r})n(\mathbf{r})d\mathbf{r}, \quad (5)$$

where $\epsilon_{xc}^{\text{approx}}$ is made to depend on $n(\mathbf{r})$, $\nabla n(\mathbf{r})$, and/or the electronic kinetic energy $\tau(\mathbf{r}) = \frac{1}{2} \sum_{i\sigma} |\nabla \Psi_{i\sigma}(\mathbf{r})|^2$. Next, we summarise the basic aspects of the most popular $E_{xc}[n]$ functionals employed for computational analysis of archetypal ferroelectric and multiferroic materials.

In local approaches (e.g., local density approximation -LDA-), E_{xc}^{approx} in Eq.(5) is calculated by considering

the exchange-correlation energy of an uniform electron gas with density $n(\mathbf{r})$, ϵ_{xc}^{unif} , which is known exactly from quantum Monte Carlo calculations [34 and 35]. In order to deal with the non-uniformity of real electronic systems, the space is partitioned into infinitesimal volume elements that are considered to be locally uniform. In semi-local approaches (e.g., generalized gradient approximation -GGA-), E_{xc} is approximated similarly to local approaches but $\epsilon_{xc}^{\text{approx}}$ is made to depend also on the gradient of $n(\mathbf{r})$ [36 and 37]. Both local and semi-local approximations satisfy some exact E_{xc} constraints and can work notably well for systems in which the electronic density varies slowly over the space (e.g., crystals). An extension of the GGA approach is provided by meta-GGA functionals, in which the non-interacting kinetic energy density is considered also as an energy functional input. An example of this latter type of functionals is the recently proposed meta-GGA SCAN [38 and 39].

Hybrid functionals comprise a combination of non-local exact Hartree-Fock and local exchange energies, together with semi-local correlation energies. The proportion in which both non-local and local exchange densities are mixed generally relies on empirical rules. The popular B3LYP approximation [40], for instance, takes a 20% of the exact HF exchange energy and the rest from the GGA and LDA functionals. Other well-known hybrid functionals are PBE0 [41] and the range-separated HSE06 proposed by Scuseria and collaborators [42]. In contrast to

local and semi-local functionals, hybrids describe the delocalisation of the exchange-correlation hole around an electron to some extent so that they partially correct for electronic self-interaction errors (which are ubiquitous in standard DFT) [43]. This technical feature is specially useful to treat strongly correlated systems containing d and f electronic orbitals (e.g., transition-metal oxide perovskites) [44–47].

B. Bond-valence and classical interatomic potentials

Using first-principles methods to describe the interactions between electrons and ions in crystals requires dedicated computational resources. In some cases, the interatomic interactions can be approximated satisfactorily by analytical functions known as classical interatomic potentials or force fields and consequently the simulations can be accelerated dramatically with respect to *ab initio* calculations. Classical interaction models contain a number of parameters that are adjusted to reproduce experimental or *ab initio* data, and their analytical expressions are constructed based on physical knowledge and intuition. The force matching method proposed by Ercolessi and Adams [48] is an example of a classical potential fitting technique that is widely employed in the fields of condensed matter physics and materials science [49–52]. Nonetheless, the ways in which classical interatomic potentials are constructed are neither straightforward nor uniquely defined and the thermodynamic intervals over which they remain reliable are limited.

A pairwise interaction model that has been employed to successfully simulate polar materials like BaTiO₃, LiNbO₃ and KNbO₃ at finite temperatures is the Coulomb–Buckingham (CB) potential, which adopts the simple form [53–56]:

$$V_{\alpha\beta}(r_{ij}) = A_{\alpha\beta} e^{-\frac{r_{ij}}{\rho_{\alpha\beta}}} - \frac{C_{\alpha\beta}}{r_{ij}^6} + \frac{Z_{\alpha}Z_{\beta}}{r_{ij}}, \quad (6)$$

where subscripts α and β represent atomic species in the system, r_{ij} the radial distance between a pair of α and β atoms labelled i and j respectively, Z ionic charges, and A , ρ and C are potential parameters. The CB potential is composed of three different energy contributions. The exponential term accounts for short-range repulsive forces resulting from the interactions between nearby electrons; the second term represents long-range attractive interactions arising from dispersive van der Waals forces; the third term is the usual Coulomb interaction between point charges. In order to describe atomic polarizability effects, “core-shell” modelling can be done on top of the CB potential. In standard core-shell approaches, each atom is decomposed into a charged core, which interact with others through V_{ij} ’s analogous to the expression shown in Eq.(6), and a charged shell that is bound harmonically to the core [54–57].

Polar materials are characterized by a delicate balance between short-range and long-range forces, which are respectively originated by complex transition metal (TM) d and oxygen (O) p electronic orbital hybridizations and Coulomb interactions between permanent electric dipoles and higher order moments [58]. The simplicity of the pairwise interaction model enclosed in Eq.(6) may not be adequate to fully grasp the complexity of the TM–O bonding, which turns out to be critical to describe ferroelectricity and other relevant functional properties correctly. Bond-valence (BV) potentials represent an improvement with respect to the CB model because they can mimic chemical bonding in oxide perovskites and other complex materials more precisely [59].

A general BV potential for oxide perovskites is [60–63]:

$$V_{\text{BV}}(r, \theta) = V_{\text{bind}}(r) + V_{\text{charge}}(r) + V_{\text{rep}}(r) + V_{\text{nl}}(\theta), \quad (7)$$

where the first term in the right-hand side represents the bond-valence potential energy, the second the Coulomb potential energy, the third the repulsive potential energy, and the fourth an angle potential energy (to prevent unphysically large distortions of the oxygen octahedra). The bond-valence energy term generally is expressed as:

$$V_{\text{bind}}(r) = \sum_{\alpha=1}^{N_s} S_{\alpha} \sum_{i=1}^{N_{\alpha}} |V_{i\alpha}(r_i) - V_{\alpha}|^{\gamma_{\alpha}}, \quad (8)$$

with

$$V_{i\alpha}(r_i) = \sum_{\beta=1}^{N_s} \sum_j^{NN} \left(\frac{r_0^{\alpha\beta}}{r_{ij}^{\alpha\beta}} \right)^{C_{\alpha\beta}}, \quad (9)$$

where N_s represents the number of atomic species in the system (e.g., 3 for PbTiO₃), S_{α} are fitting parameters, N_{α} the number of α atoms, V_{α} the desired atomic valence for ion α , γ_{α} fitting parameters typically set to 1, j an atomic index that runs over nearest-neighbour (NN) ions, $r_0^{\alpha\beta}$ and $C_{\alpha\beta}$ parameters determined by empirical rules, and $r_{ij}^{\alpha\beta}$ the radial distance between ions i and j .

For the repulsive energy term, V_{rep} , the following expression normally is employed:

$$V_{\text{rep}}(r) = \epsilon \sum_{\alpha=1}^{N_s} \sum_{i=1}^{N_{\alpha}} \sum_{\beta=1}^{N_s} \sum_{j=1}^{N_{\beta}} \left(\frac{B_{\alpha\beta}}{r_{ij}^{\alpha\beta}} \right)^{12}, \quad (10)$$

where ϵ and $B_{\alpha\beta}$ are fitting parameters. Meanwhile, an harmonic function is used for the angle potential energy that reads:

$$V_{\text{nl}}(\theta) = k \sum_{i=1}^{N_{\text{oct}}} (\theta_{i,x}^2 + \theta_{i,y}^2 + \theta_{i,z}^2), \quad (11)$$

where k is a fitting parameter, N_{oct} the number of the oxygen octahedra, and $\{\theta_{i,\gamma}\}$ the angles between the oxygen octahedral axes and the system reference axes.

Reliable BV potentials have been developed for archetypal ferroelectric and piezoelectric materials like BaTiO₃, PbTiO₃, and PbZr_{0.2}Ti_{0.8}O₃ [60–64]. Recently, it has been predicted based on the outcomes of molecular dynamics simulations performed with BV potentials that ultrafast electric-field pulses can induce giant and inverse EC effects (i.e., $\Delta T < -10$ K) in bulk BaTiO₃ and PbTiO₃ [65]. Such caloric effects occur in the time scale of few picoseconds hence they could be exploited for the design of fast solid-state cooling processes.

C. Effective Hamiltonians

Another first-principles based approach that has proven very successful in describing ferroelectric oxide perovskites is the effective Hamiltonian method [66–68]. In this approach, a subset of degrees of freedom that is relevant to the observed phase transitions is first selected. The parameters defining the effective Hamiltonian are then determined by performing accurate zero-temperature first-principles calculations. Finally, finite- T simulations are undertaken to assess displacive-like phase transition governed by the constructed effective Hamiltonian. In the effective Hamiltonian approach, the energy surface of the polar crystal is approximated by a low-order Taylor expansion of the energy surface of a high-symmetry non-polar cubic phase, which is observed in some archetypal ferroelectrics at high temperatures.

A typical effective Hamiltonian consists of five energy contributions: a local-mode self-energy, a long-range dipole-dipole interaction, a short-range interaction between soft modes, an elastic energy, and an interaction between the local modes and local strain [66]. Analytically, this model is expressed as:

$$E^{\text{tot}} = E^{\text{self}}(\{\mathbf{u}\}) + E^{\text{dipol}}(\{\mathbf{u}\}) + E^{\text{short}}(\{\mathbf{u}\}) + E^{\text{elast}}(\{\eta\}) + E^{\text{int}}(\{\eta\}, \{\mathbf{u}\}), \quad (12)$$

where $\{\mathbf{u}\}$ are the amplitude vector of the lowest-energy transversal optical Γ -phonon modes of the parent cubic phase, and $\{\eta\}$ the corresponding six-component local strain tensor.

The local-mode self-energy term adopts the form:

$$E^{\text{self}}(\{\mathbf{u}\}) = \sum_i \kappa u_i^2 + \alpha u_i^4 + \gamma (u_{ix}^2 u_{iy}^2 + u_{ix}^2 u_{iz}^2 + u_{iy}^2 u_{iz}^2), \quad (13)$$

where $u_i = |\mathbf{u}_i|$ and κ , α and γ are expansion parameters to be determined from first-principles calculations. For the long-range energy term, only dipole-dipole interactions are considered and the following expression is employed:

$$E^{\text{dipol}}(\{\mathbf{u}\}) = \frac{\mathcal{Z}^2}{\epsilon_\infty} \sum_{i < j} \frac{\mathbf{u}_i \mathbf{u}_j - 3(\hat{\mathbf{r}}_{ij} \mathbf{u}_i)(\hat{\mathbf{r}}_{ij} \mathbf{u}_j)}{r_{ij}^3}, \quad (14)$$

where \mathcal{Z} is the Born effective charge associated with the soft mode, ϵ_∞ the optical dielectric constant of the material, $\mathbf{r}_{ij} \equiv \mathbf{r}_i - \mathbf{r}_j$ the distance vector between different unit cells, and $\hat{\mathbf{r}}_{ij} \equiv \mathbf{r}_{ij}/r_{ij}$. To express the short-range interactions between neighboring local modes, a formula that is reminiscent of the spin Heisenberg model is adopted:

$$E^{\text{short}}(\{\mathbf{u}\}) = \frac{1}{2} \sum_{i \neq j} \sum_{\alpha \beta} J_{ij, \alpha \beta} u_{i\alpha} u_{j\beta}, \quad (15)$$

which typically applies to first, second and third neighbouring unit cells, and where the coupling matrix $J_{ij, \alpha \beta}$ depends on r_{ij} and decays rapidly with increasing distance. Meanwhile, the elastic energy and elastic-mode interaction energy terms are deduced by considering symmetry and stress-strain relationships of the parent cubic phase (e.g., elastic constants). For instance, $E^{\text{elast}}(\{\eta\})$ is expressed as a sum of homogeneous and inhomogeneous deformations that allow to change the shape and volume of the simulation cell, while the elastic-mode interaction energy adopts the form:

$$E^{\text{int}}(\{\eta\}, \{\mathbf{u}\}) = \frac{1}{2} \sum_i \sum_{l\alpha\beta} B_{l\alpha\beta} \times \eta_l(\mathbf{r}_i) u_\alpha(\mathbf{r}_i) u_\beta(\mathbf{r}_i), \quad (16)$$

where $B_{l\alpha\beta}$ are strain-mode coupling constants.

To put some numbers on the construction of the E^{tot} functional expressed in Eq.(12), a total of 18 expansion parameters estimated with first-principles methods are required to obtain a minimum reliable effective Hamiltonian model for BaTiO₃ [66]. Depending on the material and physical phenomena to be simulated more complexity can be added to the E^{tot} expression, although the number of involved expansion parameters can increase very rapidly [67 and 68]. A version of the effective Hamiltonian approach for oxide perovskite has been already implemented in the freely available code package FeRam [25].

Effective Hamiltonians, as any other method, present some limitations. First, because they focus on certain degrees of freedom they may not be accurate enough to capture the full range of behavior of the material under study, especially for configurations beyond the model training database. Second, an appropriate selection of the degrees of freedom requires significant insight into the material, which may retard the development of such models for new systems. Third, first-order phase transitions characterised by large symmetry and volume changes cannot be simulated with effective Hamiltonians (recall the fundamental approximation of a low-order Taylor expansion around a presumed reference cubic phase). And fourth, the connectivity between atoms needs to be fixed for all the simulated phases thus variations in the atomic environment cannot be reproduced.

Recently, an extension of the effective Hamiltonian method has been developed, the so-called “second-

principles” approach, which may overcome some of the technical issues just mentioned [26 and 69]. In the second-principles approach, the parameters of the effective Hamiltonian model are computed in a very fast and efficient way by recasting the E^{tot} fit to a training set of first-principles data into a simple matrix diagonalization problem. Specifically, the interactions that are most relevant to reproduce the first-principles training-set data are selected automatically from a pool that virtually includes all possible coupling terms. The second-principles method has been already implemented in the freely available code package SCALE-UP [26].

III. INDIRECT ESTIMATION OF THE EC EFFECT

The isothermal entropy change that a polar material undergoes under the action of a varying external electric field can be expressed by means of the Maxwell relations as [10]:

$$\Delta S(T, \mathcal{E}_f) = \int_0^{\mathcal{E}_f} \left(\frac{dP}{dT} \right)_{\mathcal{E}} d\mathcal{E}, \quad (17)$$

where P represents the electric polarization of the system and \mathcal{E} the applied electric field. Likewise, the corresponding adiabatic temperature shift can be estimated as:

$$\begin{aligned} \Delta T(T, \mathcal{E}_f) &= - \int_0^{\mathcal{E}_f} \frac{T}{C_{\mathcal{E}}(T)} dS \\ &\approx - \frac{T}{C_0(T)} \Delta S(T, \mathcal{E}_f), \end{aligned} \quad (18)$$

where $C_{\mathcal{E}}(T) \equiv \left(\frac{dU}{dT} \right)_{\mathcal{E}}$ is the heat capacity of the system at fixed electric field \mathcal{E} and U the internal energy. Typically, ΔS and ΔT are large in the vicinity of a \mathcal{E} -induced phase transition because at such conditions the T -induced variation of P is most significant.

Equations (17) and (18) show that the isothermal entropy and adiabatic temperature shifts associated with the electrocaloric (EC) effect can be estimated indirectly by knowing the heat capacity of the system and the pyroelectric coefficient, $\alpha_{\mathcal{E}} \equiv \left(\frac{dP}{dT} \right)_{\mathcal{E}}$. As we explain next, indirect estimation of EC effects can be achieved theoretically by using (i) classical interaction potentials and effective Hamiltonian models in classical molecular dynamics and Monte Carlo simulations, and (ii) first-principles methods in combination with quasi-harmonic approaches (Sec.II and Fig.1). It is worth noting that indirect estimation of EC effects is only meaningful in the context of second-order phase transitions since otherwise the pyroelectric coefficient $\alpha_{\mathcal{E}}$ is ill defined at the transition point and consequently Eq.(17) cannot be estimated numerically (see next section for the estimation of EC effects associated with first-order phase transitions).

In both molecular dynamics (MD) and Monte Carlo (MC) simulations it is possible to simulate the system of

interest at the desired T , \mathcal{E} and pressure (or volume) conditions. MD simulations are deterministic and rely on the numerical discretization and integration of Newton’s second law of motion [70]. MC simulations, by contrast, are stochastic and rely on efficient sampling of the Maxwell-Boltzmann probability distribution [71]. Nevertheless, when the technical parameters in MD and MC simulations are selected to ensure proper convergence the average results obtained in both types of simulations should be equivalent. Typically, large system sizes ($N \sim 10^3 - 10^7$) and long simulation times ($\tau \sim 1 - 10$ ns) are required to obtain well converged results in MD and MC simulations. As a consequence, first-principles methods normally are excluded from such type of finite- T approaches and bond valence/classical interaction potentials and effective Hamiltonians remain as the *ab initio* based alternatives for modelling the interatomic interactions [28, 29, 72, and 73].

The heat capacity and pyroelectric coefficient of a polar crystal can be estimated efficiently with both MD and MC methods by computing average internal energies and atomic positions (or local modes) in simulations performed at different temperatures. Alternatively, ΔS can be estimated in a quasi-direct fashion by integrating the specific heat obtained at constant electric field like:

$$\Delta S(T, \mathcal{E}_f) = \int_{T_0}^T \frac{C_0(T') - C_{\mathcal{E}_f}(T')}{T'} dT', \quad (19)$$

where T_0 needs to be sufficiently low in practice so that the condition $S(T_0, 0) \approx S(T_0, \mathcal{E}_f)$ is fulfilled [72]. In the context of effective Hamiltonians, the following expression also can be used to estimate adiabatic temperature shifts produced by electric fields [29]:

$$\Delta T(T, \mathcal{E}_f) = -\gamma_T \int_0^{\mathcal{E}_f} \frac{\langle u \cdot U \rangle - \langle u \rangle \cdot \langle U \rangle}{\langle U^2 \rangle - \langle U \rangle^2} d\mathcal{E}, \quad (20)$$

where $\gamma_T \equiv \mathcal{Z} a_0 N T$, \mathcal{Z} is the Born effective charge associated with the soft mode, a_0 the lattice parameter of the cubic unit cell, N the number of sites in the supercell, u the module of the average supercell local mode, U the total energy, and $\langle \dots \rangle$ denotes thermal average.

Despite the high computational cost associated with first-principles methods, it is also possible to estimate EC effects indirectly with them by means of the quasi-harmonic approximation (QHA). In the quasi-harmonic approach, the internal energy of a crystal is expressed as [74–76]:

$$E_{\text{harm}}(T) = E_0 + \frac{1}{2} \sum_{mn} \Xi_{mn} u_m(T) u_n(T), \quad (21)$$

where E_0 corresponds to the static energy, Ξ_{mn} the force-constant matrix and $\{u\}$ atomic displacements that depend on T . The phonon frequencies of the crystal, $\{\omega_{\mathbf{q}s}\}$, and corresponding normal mode amplitudes, $\{Q_{\mathbf{q}s}\}$, are calculated from the diagonalization of the dynamical ma-

trix obtained from Ξ_{mn} .

According to well-established theories [77], the pyroelectric coefficient of a crystal subject to constant stress, σ , can be decomposed into two contributions: the primary contribution obtained at constant strain, $\alpha_{\mathcal{E}(\eta)}$, and the secondary contribution associated with the material thermal expansion, $\alpha_{\mathcal{E}(T)}$. These two parts can be expressed analytically as [78 and 79]:

$$\alpha_{\mathcal{E}} = \alpha_{\mathcal{E}(\eta)} + \alpha_{\mathcal{E}(T)} = \left(\frac{\partial P}{\partial T} \right)_{\eta} + \sum_i \left(\frac{\partial P}{\partial \eta_i} \right)_T \left(\frac{d\eta_i}{dT} \right)_{\sigma}. \quad (22)$$

The secondary contribution to $\alpha_{\mathcal{E}}$ corresponds to the pyroelectricity induced by the thermal expansion, which can be obtained from the material piezoelectric stress constants and volume expansion coefficients computed with first-principles methods. The primary contribution to $\alpha_{\mathcal{E}}$ corresponds to the ‘‘clamped-lattice’’ pyroelectricity, which results from holding the lattice parameters of the crystal fixed.

The electric polarization can be expanded in terms of the vibrational normal mode amplitudes, $\{Q_{\mathbf{q}s}\}$, according to the formula [78–80]:

$$P(T) = P(0) + \sum_{\mathbf{q}s} \frac{\partial P}{\partial Q_{\mathbf{q}s}} \langle Q_{\mathbf{q}s} \rangle, \quad (23)$$

where the first term represents the electric polarization in the absence of thermal fluctuations, which can be readily calculated with first-principles methods [81]. The primary contribution to the pyroelectric coefficient in Eq.(22) then can be expressed as [78–80]:

$$\alpha_{\mathcal{E}(\eta)} = \sum_s \frac{\partial P}{\partial Q_{\Gamma_s}} \frac{d\langle Q_{\Gamma_s} \rangle}{dT} + \sum_{\mathbf{q}s} \frac{\partial^2 P}{\partial Q_{\mathbf{q}s}^2} \frac{d\langle Q_{\mathbf{q}s}^2 \rangle}{dT}, \quad (24)$$

where only polar Γ -optical survive in the first term. By using the QHA and first-principles simulations, one can estimate the temperature derivatives in Eq.(24) via the expressions [78 and 79]:

$$\langle Q_{\Gamma_s} \rangle = \sum_{\mathbf{q}l} \frac{\hbar}{2} \frac{(2n_{\mathbf{q}l} + 1)}{\omega_{\Gamma_s}^2} \frac{\partial \omega_{\mathbf{q}l}}{\partial Q_{\Gamma_s}} \quad (25)$$

$$\langle Q_{\mathbf{q}s}^2 \rangle = \frac{\hbar}{2} \frac{(2n_{\mathbf{q}s} + 1)}{\omega_{\mathbf{q}s}}, \quad (26)$$

where n is the Bose–Einstein distribution function, which depends explicitly on the temperature [74]. The pyroelectric properties of several semiconductor (e.g., GaN and ZnO [29]) and two-dimensional materials (e.g., GeS and MoSSe [73]) have been estimated successfully with the explained combination of *ab initio* methods and the quasi-harmonic approach.

Likewise, the heat capacity of a crystal can be estimated within the quasi-harmonic approximation by using

the formula [9]:

$$C_0(T) = \frac{1}{N_q} \sum_{\mathbf{q}s} \frac{(\hbar \omega_{\mathbf{q}s})^2}{k_B T^2} \frac{e^{\frac{\hbar \omega_{\mathbf{q}s}}{k_B T}}}{\left(e^{\frac{\hbar \omega_{\mathbf{q}s}}{k_B T}} - 1 \right)^2}, \quad (27)$$

where N_q is the total number of wave vectors used for integration in the first Brillouin zone and the summation runs over all wave vectors \mathbf{q} and phonon branches s . Thus, by using Eqs.(22)–(27), that is, by determining $\alpha_{\mathcal{E}}$ and C_0 and their dependence on temperature, in principle it is possible to estimate EC effects indirectly with first-principles methods and remarkable accuracy without the need to perform finite- T MD or MC simulations.

IV. CLAUSIUS-CLAPEYRON METHOD

In the case that the \mathcal{E} -field induced phase transition of interest presents a marked first-order character, the corresponding isothermal entropy change can be estimated with the Clausius-Clapeyron method as [10]:

$$\Delta S(T) = -\Delta P(T) \frac{d\mathcal{E}_c}{dT}, \quad (28)$$

where $\Delta P(T)$ is the change in polarization along the electric field direction, and $\mathcal{E}_c(T)$ the critical electric field inducing the phase transformation.

In the presence of an electric field and by assuming zero-pressure conditions, the thermodynamic potential that appropriately describes the stability of a particular phase is the Gibbs free energy defined as $G = F - \mathcal{E} \cdot \mathbf{P}$, where F represents the Helmholtz free energy (where $F \equiv U - TS$ and U is the internal energy). Accordingly, the thermodynamic condition that determines the \mathcal{E} -induced phase transition between states A and B is $G^A(T, \mathcal{E}_c) = G^B(T, \mathcal{E}_c)$. The approximate value of the corresponding critical electric field then can be estimated as:

$$\mathcal{E}_c(T) \approx \frac{\Delta F(T)}{\Delta P(T)}, \quad (29)$$

where ΔF represents the Helmholtz free energy difference between the two states, and ΔP their electric polarization difference along the electric field direction. By knowing $\Delta F(T)$ and $\Delta P(T)$, then one can calculate ΔS and, if the heat capacity of the system is also known, ΔT as a function of temperature.

The Helmholtz free energy of the competing polymorphs in some cases can be estimated accurately as a function of temperature with first-principles methods and the quasi-harmonic approximation (QHA) [74–76]. In particular, the Helmholtz free energy associated with the lattice vibrations, F_{vib} , is calculated by finding the phonon frequencies of the crystal, $\{\omega_{\mathbf{q}s}\}$, and subse-

quently using the formula:

$$F_{\text{vib}}(T) = \frac{1}{N_q} k_B T \sum_{\mathbf{q}s} \ln \left[2 \sinh \left(\frac{\hbar \omega_{\mathbf{q}s}}{2k_B T} \right) \right], \quad (30)$$

where N_q is the total number of wave vectors used for integration in the first Brillouin zone, and the summation runs over all wave vectors \mathbf{q} and phonon branches s . The total Helmholtz free energy of the system finally can be estimated as:

$$F_{\text{harm}}(T) = E_0 + F_{\text{vib}}(T), \quad (31)$$

where E_0 is the static energy calculated with the atoms frozen on their equilibrium lattice positions.

Since the electric polarization difference between polymorphs A and B and their heat capacities also can be estimated as a function of temperature within the quasi-harmonic approximation (Sec.III), the adiabatic temperature and isothermal entropy changes in Eqs.(18) and (28) in principle can be determined with first-principles methods. In fact, the described QHA method has been employed recently to predict large EC effects in multiferroic BiCoO₃ thin films caused by abrupt first-order phase transitions [27] (this illustrative case will be explained in detail in Sec.VI A).

Nevertheless, anharmonic effects, which mostly are not accounted for by quasi-harmonic approaches, can be very important in ferroelectric materials (e.g., BaTiO₃) and consequently the QHA may not be adequate to describe them correctly (for instance, when imaginary frequencies appear in the vibrational phonon spectra Eq.(30) cannot be used [74]). In this case, one still can employ genuine *ab initio* methods to compute anharmonic free energies for the relevant polymorphs with methods like thermodynamic integration from reference models [82–84] and self-consistent phonon approaches [85–87]. The computational load associated with these latter *ab initio* anharmonic methods, however, is huge and to the best of our knowledge they have not been used for the simulation of EC effects to this day.

V. DIRECT ESTIMATION OF THE EC EFFECT

MD and MC simulations allow to estimate EC effects directly, that is, by avoiding the use of the Maxwell relations. This modality of EC simulation may be beneficial for cases in which (i) the definition of the electric polarization poses some ambiguity (e.g., disordered crystals [20]), and/or (ii) the polar degrees of freedom are strongly coupled with the lattice strain (e.g., good piezoelectric materials) since in that case Eq.(17) neglects possible secondary EC effects arising from \mathcal{E} -induced structural distortions [18]. On the other hand, this type of simulations only can be performed feasibly with classical interatomic/bond valence potentials and effective Hamiltonians because involve explicit simulation of $T \neq 0$ con-

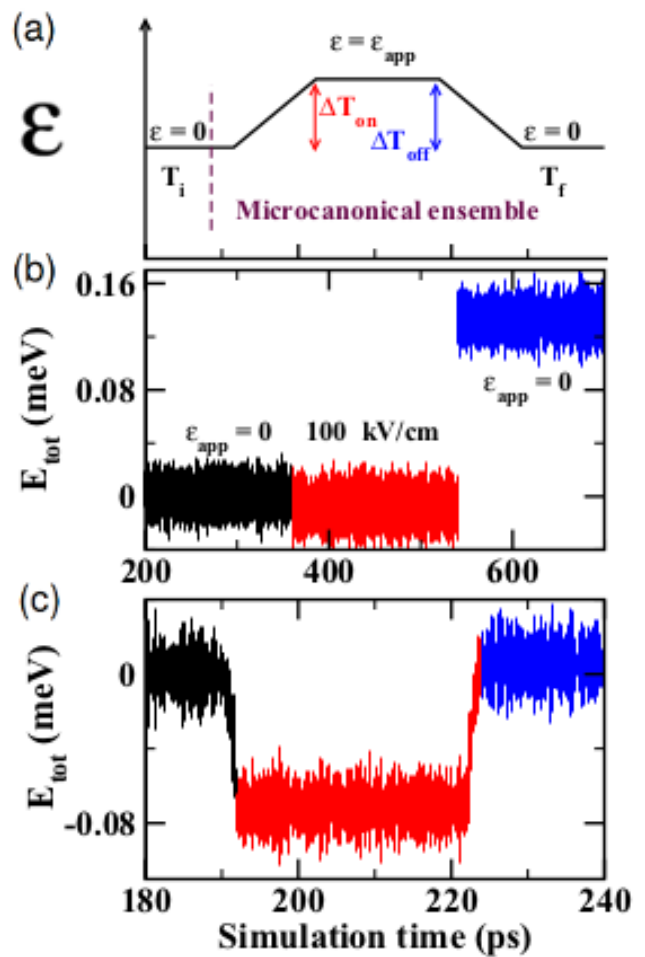


FIG. 2: (a) Sketch of the simulation \mathcal{E} -ramping protocol employed for direct estimation of EC effects. Total energy of the system as a function of MD steps for (b) instantaneous field switching on/switching off and (c) slow field ramping, respectively. The process simulated in (b) is irreversible and in (c) practically reversible. Reproduced from work [72].

ditions, and apply exclusively to EC effects deriving from second-order phase transitions.

Direct estimation of EC effects have been performed for a number of different systems including hybrid organic-inorganic perovskites [28] and multifunctional oxides [29, 65, 72, and 73]. In this type of simulations, the electric field needs to be applied/removed very slowly so that the electrical polarization can follow adiabatically the external field. On the contrary, the simulated EC process is irreversible to some extent and the resulting adiabatic temperature shifts are not meaningful (Fig.2).

Initially, the system is thermalized at the temperature of interest, T_i , and zero electric field in the canonical, (N, V, T) , or the isobaric-isothermal, (N, p, T) , ensemble (where p represents the hydrostatic pressure). After thermalization, the simulation is switched to the microcanonical or the isoenthalpic-isobaric ensemble $[(N, E, V)$ or

(N, H, p) where E and H represent the internal energy and enthalpy, respectively]. At this stage the electric field is ramped up to the desired value slowly enough to guarantee adiabaticity, and the accompanying temperature change, ΔT_{on} , is monitored. The system is simulated under these conditions for some time. Subsequently, the electric field is ramped down to zero slowly enough again to guarantee adiabaticity and the corresponding temperature change, ΔT_{off} , and final temperature, T_f , are monitored.

Under the condition that the system remains in thermal equilibrium during the entire described simulation cycle, it will follow that $T_i = T_f$ and $\Delta T_{\text{on}} = \Delta T_{\text{off}}$ within their corresponding statistical uncertainties (Fig.2c and [72]). In such a case, either ΔT_{on} or ΔT_{off} can be identified with the adiabatic temperature change associated with the simulated EC process.

VI. REPRESENTATIVE EXAMPLES

In this section, we describe three illustrative cases in which original EC effects have been simulated and quantified with first-principles based methods. The systems in which those EC effects have been predicted are technologically relevant, namely, multiferroic BiCoO_3 thin films (*ab initio* methods in combination with the quasi-harmonic approximation), the organic-inorganic halide perovskite $\text{CH}_3\text{NH}_3\text{PbI}_3$ (classical force fields and molecular dynamics simulations) and the relaxor ferroelectric $\text{BaZr}_{1-x}\text{Ti}_x\text{O}_3$ (effective Hamiltonians and molecular dynamics and Monte Carlo simulations). Analogous EC simulation success can be achieved for other similar polar materials.

A. Multiferroic BiCoO_3 thin films

In multiferroic materials several order parameters coexist, typically ferroelectricity and magnetism, and are coupled to each other. Such unique properties convert multiferroics into promising materials for applications in memory devices, sensors and solid state cooling [9], to cite few examples. The archetypal multiferroic compound is the oxide perovskite BiFeO_3 , which presents a rhombohedral ground-state phase characterised by an electric polarisation of $\sim 60 \mu\text{C}/\text{cm}^2$ and antiferromagnetic (AFM) spin ordering of G-type [2] (Fig.3).

Bulk BiCoO_3 (BCO) is another multiferroic material in which ferroelectricity and antiferromagnetism coexist at ambient conditions. The stable phase of BCO is ferroelectric (FE) and tetragonal \mathcal{T} , with a significantly large out-of-plane versus in-plane lattice constant ratio of ≈ 1.3 (Fig.3) [3 and 27]. The competing structures in BCO are the paraelectric (PE) orthorhombic \mathcal{O} phase and the FE monoclinic \mathcal{M} phase [3]. Both competitive phases have cells that are slightly distorted versions of the ideal cubic perovskite structure, with $c/a \approx 1$. The

mentioned FE phases present spontaneous polarizations along quite different crystallographic directions, namely, pseudocubic $[001]_{\text{pc}}$ for \mathcal{T} and $\sim [111]_{\text{pc}}$ for \mathcal{M} (Fig.3). As regards magnetism, both the \mathcal{O} and \mathcal{M} phases display G-type AFM order (Fig.3) with a quite high Néel temperature $T_N \sim 500$ K. The \mathcal{T} phase, on the contrary, presents C-type AFM order (Fig.3) with a relatively low $T_N \sim 310$ K [3 and 27].

The competition between BCO polymorphs is strongly affected by epitaxial strain, which is realized in practice by growing epitaxially thin films on perovskite substrates, as this imposes an in-plane lattice constant a_{in} in the system. At zero-temperature conditions, a strain-driven $\mathcal{T} \rightarrow \mathcal{M}$ phase transformation has been predicted to occur at $a_{\text{in}} = 3.925 \text{ \AA}$ that involves rotation of the polarization and the appearance of anti-phase oxygen octahedral rotations along the three pseudocubic directions [27]. The \mathcal{O} phase remains close in energy to the \mathcal{M} polymorph over the whole a_{in} interval but never becomes stable at zero temperature. Meanwhile, the Néel temperature of epitaxially grown BCO thin films decreases mildly with increasing a_{in} [27].

Cazorla and Íñiguez have performed first-principles Helmholtz free-energy calculations within the quasi-harmonic approximation for the three relevant BCO polymorphs to determine their relative stability as a function of T and a_{in} (Sec.IV) [27]. The predicted T - a_{in} phase diagram for epitaxially grown BCO thin films is shown in Fig.4a. For relatively small a_{in} 's, it is found that the \mathcal{T} phase dominates and extends its stability region to temperatures much higher than observed in bulk BCO [3]. The reason for this \mathcal{T} stability enhancement is that the competing \mathcal{O} polymorph remains highly strained at such a_{in} conditions, hence its free energy increases considerably as compared to the bulk case. As a_{in} is increased, the \mathcal{T} phase eventually is replaced by the \mathcal{O} and \mathcal{M} polymorphs, yielding a very rich phase diagram that exhibits concurrent structural and spin-ordering transformations.

Figures 4b-d show the calculated Helmholtz free-energy differences $\Delta \tilde{F}_{\text{harm}}$ between the three relevant BCO polymorphs expressed as a function of T and a_{in} [27]. Those calculations take into account all possible sources of entropy, namely, magnetic and vibrational, and the interplay between spin disorder and lattice vibrations. It is found that at high temperatures ($T \gtrsim 600$ K) the vibrational contributions to \tilde{F}_{harm} always favor the \mathcal{O} and \mathcal{M} phases over the \mathcal{T} phase. Nevertheless, whenever a polymorph becomes magnetically disordered, the corresponding Helmholtz free energy decreases significantly as a consequence of T -induced lattice phonon softening [27]. Accordingly, abrupt $\Delta \tilde{F}_{\text{harm}}$ changes appear in Figs.4b-d at the corresponding AFM \rightarrow PM magnetic transition temperatures. The strong spin-phonon couplings in epitaxially grown BCO thin films are responsible for the stabilization of the \mathcal{O} -AFM(G) phase at temperatures near ambient and $3.88 \text{ \AA} \leq a_{\text{in}} \leq 3.96 \text{ \AA}$. Indeed, when spin-phonon couplings are disregarded the \mathcal{O} phase becomes stable only at high temperatures when reaches

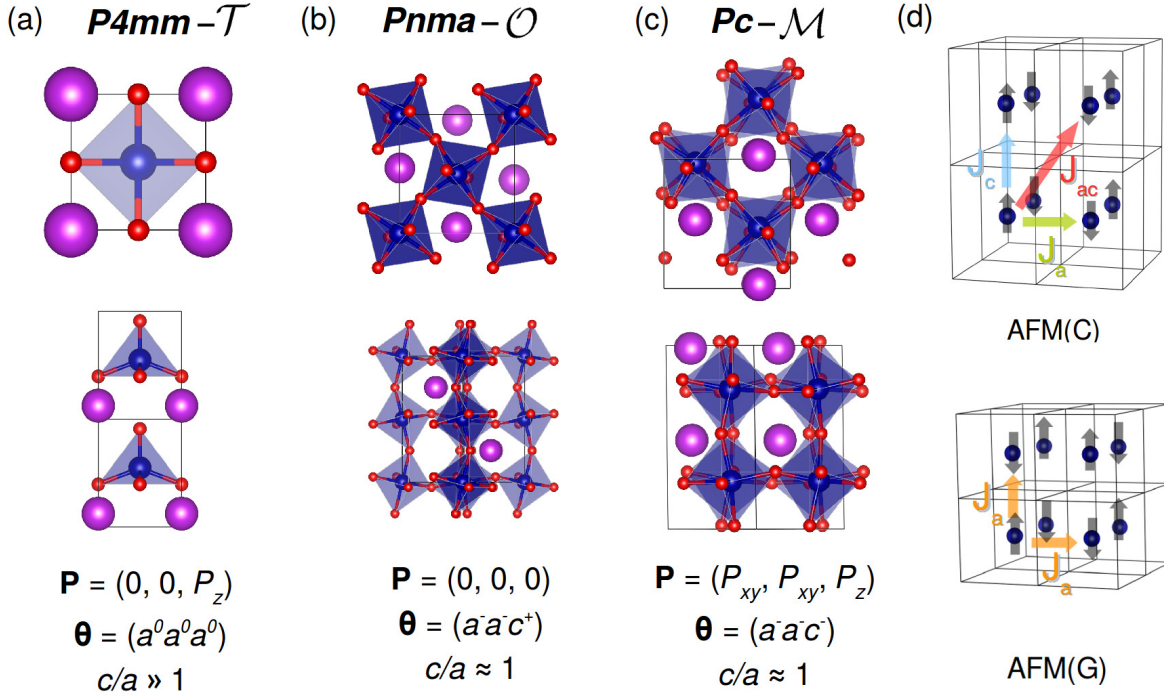


FIG. 3: Structural, ferroelectric, and magnetic properties of energetically competitive bulk BCO polymorphs. (a) Tetragonal $P4mm$ (\mathcal{T}), (b) orthorhombic $Pnma$ (\mathcal{O}), and (c) monoclinic Pc (\mathcal{M}). (d) Sketch of the spin configurations and exchange constants considered for the \mathcal{T} -AFM(C) and \mathcal{O} -AFM(G) Heisenberg spin models. Electrical polarizations \mathbf{P} are referred to pseudocubic Cartesian axis, and oxygen-octahedra rotation patterns $\boldsymbol{\theta}$ are expressed in Glazer's notation. Reproduced from work [27].

the paramagnetic state (Figs.4b–d) [27].

The a_{in} region $3.89 \text{ \AA} \leq a_{\text{in}} \leq 3.93 \text{ \AA}$ is particularly relevant from a practical perspective since many perovskite substrates present lattice constants in this range. Interestingly, a \mathcal{T} -induced reentrant behavior that is reminiscent of bulk BCO under compression [3] occurs therein: upon heating, the BCO film transforms first from a FE (\mathcal{T} -AFM(C) or \mathcal{M} -AMF(G)) phase to a PE (\mathcal{O} -AFM(G)) state, then back to a FE (\mathcal{T} -PM) phase, and finally to a PE (\mathcal{O} -AFM(G)) state. Of particular interest is the PE \mathcal{O} -AFM(G) region appearing near room temperature T_{room} , which is surrounded by two FE phase domains presenting markedly different features. In particular, the phase diagram in Fig.4a suggests that the \mathcal{O} phase may be transformed into the \mathcal{T} or \mathcal{M} states by applying an electric field \mathcal{E} along the $[001]_{\text{pc}}$ or $[111]_{\text{pc}}$ directions, respectively. Such \mathcal{E} -driven phase transformations involve drastic structural changes as well as magnetic transitions, hence big entropy changes are likely to occur as a consequence.

Figure 5 shows the direct EC effect associated with the field-induced $\mathcal{O} \rightarrow \mathcal{M}$ transformation (Fig.5a), in which the entropy of the system decreases ($\Delta S < 0$, Fig.5c). Since the critical temperature for the ferroelectric-paraelectric phase transition in BCO is close to 1,000 K [3], thermal effects on the electric polarization can be disregarded near room temperature [i.e.,

$\Delta P(T) \approx \Delta P(0)$ in Eqs.(28) and (29)]. For the smallest a_{in} values, a maximum adiabatic temperature change ΔT of +10 K (Fig.5d) is estimated for a maximum critical electric field of 110 kVcm^{-1} (Fig.5b). The magnitude of this effect and of the accompanying critical electric field decrease with increasing a_{in} , as the region of \mathcal{M} stability is approached. Similarly, Fig.5 shows the inverse EC effect associated with the field-induced $\mathcal{O} \rightarrow \mathcal{T}$ transformation (Fig.5a), in which the entropy of the film increases ($\Delta S > 0$, Fig.5c). A maximum ΔT of -50 K (Fig.5d) is estimated for a maximum critical electric field of 500 kVcm^{-1} at $a_{\text{in}} = 3.93 \text{ \AA}$ (Fig.5b). The magnitude of this effect and of the corresponding \mathcal{E}_c decrease with decreasing a_{in} , as the region of \mathcal{T} stability is approached.

The predicted giant ΔT and ΔS values, which can be achieved with relatively small driving fields, turn epitaxially grown BCO thin films into very attractive EC materials. For instance, the coexistence of direct and inverse EC effects suggests a possible refrigeration cycle based on the direct transformation between the high-entropy FE \mathcal{T} and the low-entropy FE \mathcal{M} phases as induced by \mathcal{E} rotation, with a cooling performance equal to the sum of the individual $\mathcal{O} \leftrightarrow \mathcal{T}$ and $\mathcal{O} \leftrightarrow \mathcal{M}$ cycles. Moreover, chemical substitution appears to be an alternative strategy for stabilizing phases that are similar to the \mathcal{M} (alike to the ground state of BiFeO_3 [81]) and \mathcal{O} (the most common among perovskites [88]) polymorphs discussed

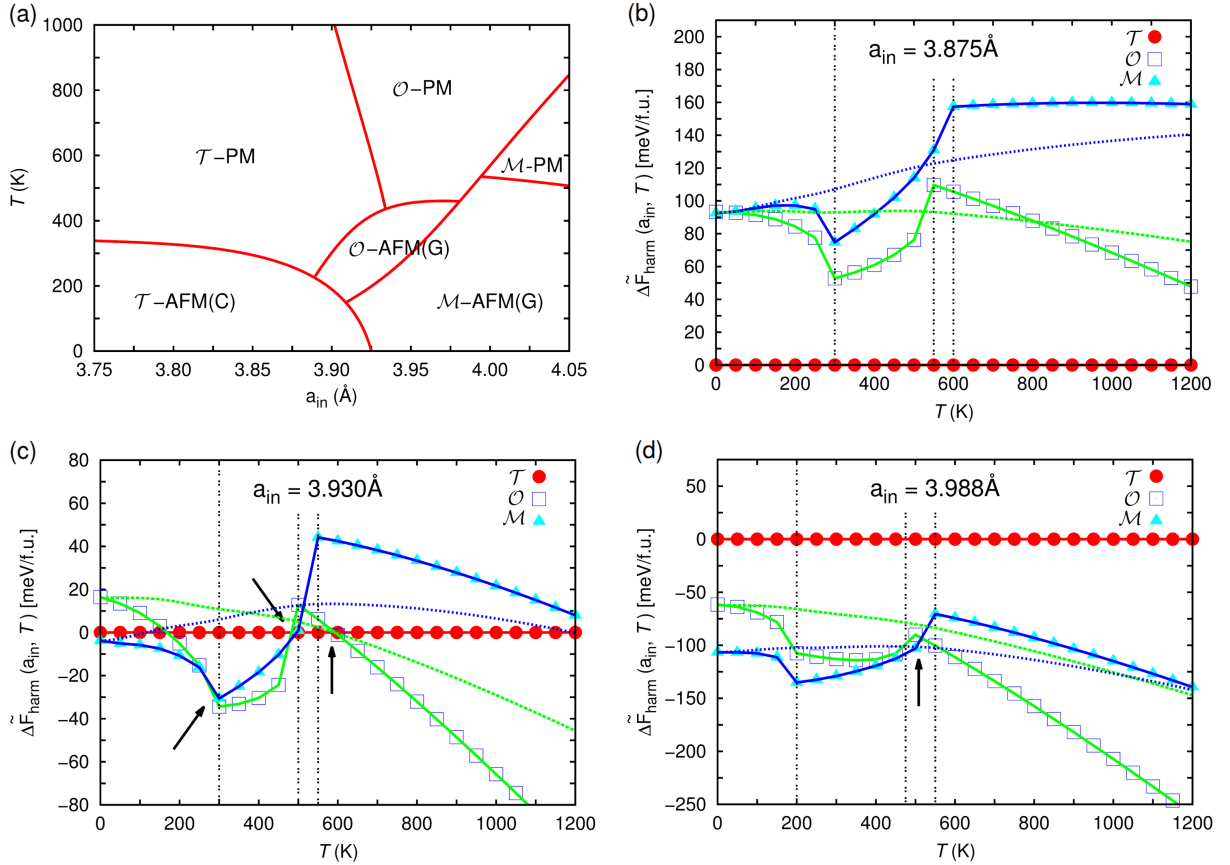


FIG. 4: T - a_{in} phase diagram and free-energy differences in (100)-oriented BCO thin films. (a) Phase diagram as a function of temperature and in-plane lattice parameter. (b) Helmholtz free-energy differences among competitive polymorphs at $a_{\text{in}} = 3.875 \text{ \AA}$, (c) $a_{\text{in}} = 3.930 \text{ \AA}$, (d) $a_{\text{in}} = 3.988 \text{ \AA}$. Vertical lines and black arrows indicate T -induced magnetic and structural phase transitions, respectively. Blue and green dotted lines correspond to Helmholtz free-energy differences for the M and O phases, respectively, calculated without considering spin-phonon coupling effects. Reproduced from work [27].

here, and to control the corresponding magnetic transition temperatures. One particular example is provided by $\text{BiCo}_{1-x}\text{Fe}_x\text{O}_3$ solid solutions, where a morphotropic transition between a T -like and a M -like phase is observed to occur at room temperature [89 and 90]. Likewise, bulk $\text{Bi}_{1-x}\text{La}_x\text{CoO}_3$ appears to be a good candidate where to realize field-driven $O \rightarrow T$ transformations [3]. Hence BCO offers a variety of experimental possibilities to achieve giant EC, bringing new exciting prospects to the field of solid-state cooling.

B. Bulk hybrid perovskite $\text{CH}_3\text{NH}_3\text{PbI}_3$

Hybrid halide perovskites described with the general chemical formula ABX_3 ($X = \text{F}, \text{Cl}, \text{Br}, \text{or I}$) consist of inorganic BX_6 octahedra, with B ions typically being Pb or Sn, and A organic molecular cations (e.g., CH_3NH_3 , see Fig.6a). The archetypal hybrid halide perovskite is $\text{CH}_3\text{NH}_3\text{PbI}_3$ (MAPbI₃), which has received a lot of attention in the past decade owing to its desirable solar

matching optical bandgap, long carrier lifetime and diffusion length and some other remarkable functional properties [91–93].

Halide perovskites in general (e.g., $\text{HC}(\text{NH}_2)_2\text{PbBr}_3$ and $\text{MD-NH}_4\text{I}_3$ [94]) display elementary properties that are not observed in the analogous perovskite oxides, such as structural softness, lightweight, and low synthesis temperatures [95]. On the other hand, the existence of ferroelectricity in halide perovskites remains a controversial and long-lasting topic of research. For instance, piezoelectric force microscopy and scanning electron microscopy studies have reported polar domains in tetragonal MAPbI₃, and weak ferroelectricity has been suggested by dielectric, piezoelectric and second harmonic generation measurements [96]. However, traditional methods that identify ferroelectric insulators convincingly fail to characterize the polar properties of MAPbI₃ due to the technical difficulties encountered in the distinction between ferroelectric and ferroelastic domains in this material [97].

At temperatures slightly above ambient conditions,

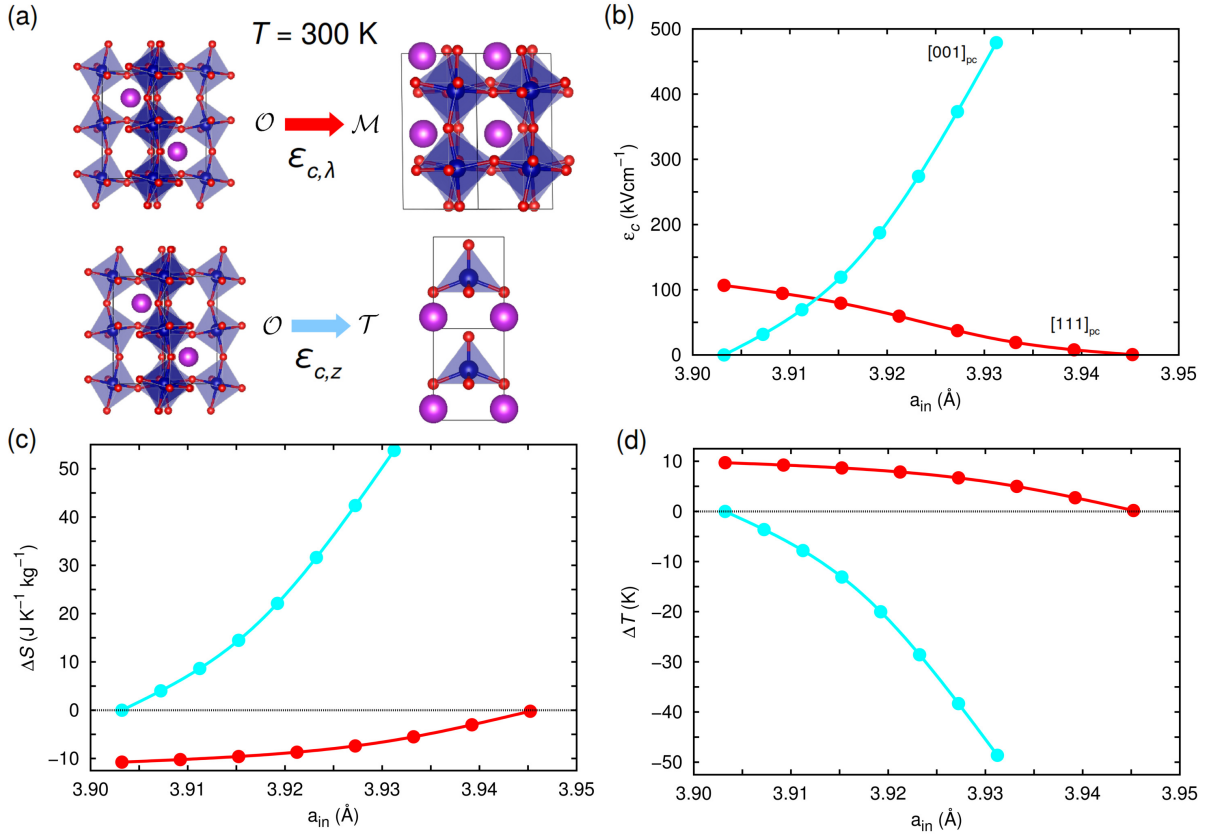


FIG. 5: Direct ($\mathcal{O} \rightarrow \mathcal{M}$, red) and inverse ($\mathcal{O} \rightarrow \mathcal{T}$, blue) electrocaloric effects in (100)-oriented BCO thin films at room temperature estimated with first-principles methods and the Clausius-Clapeyron approach. (a) Sketch of the \mathcal{E} -induced phase transformations. (b) Critical electric field expressed as a function of in-plane lattice parameter; the two involved electric field orientations are indicated in pseudocubic Cartesian notation. (c) Room-temperature entropy and (d) adiabatic temperature shifts expressed as a function of in-plane lattice parameter. Reproduced from work [27].

MAPbI₃ adopts a highly-symmetric cubic phase (space group $Pm\bar{3}m$) that is centrosymmetric and consequently cannot exhibit macroscopic electric polarization. Meanwhile, neutron powder diffraction experiments have shown that at room temperature the molecular cations in MAPbI₃, MA, are rotationally disordered [98]. Consistently, both *ab initio* and classical molecular dynamics simulations have revealed fast reorientational dynamics of the molecular cations with small relaxation times of ~ 1 ps near room temperature [50, 99, and 100].

It is worth noticing that the MA cations in MAPbI₃ carry an intrinsic electric dipole since individually they do not fulfill inversion symmetry. Therefore, under the action of an external electric field the MA rotations can be partially frustrated and the molecular cations aligned, thus inducing some sort of polar ordering. Such a \mathcal{E} -induced MA ordering effect could potentially lead to large EC effects due to the concomitant reduction in the orientational entropy of the molecular cations. Actually, colossal caloric effects near room temperature (i.e., $|\Delta T| \approx 50$ K) stemming from similar molecular ordering mechanisms, although induced by hydrostatic pressure, have

been reported recently for plastic crystals with orientational disorder like neopentylglycol, $(\text{CH}_3)_2\text{C}(\text{CH}_2\text{OH})_2$ [101–104].

Liu and Cohen have employed MD simulations and classical force fields to investigate how molecular ordering in MAPbI₃ responds to external electric fields, and what EC effects result from the accompanying polar response [28]. In particular, the authors used a standard AMBER force field recently developed by Mattoni *et al.* [50] to estimate directly (Sec.V) room temperature EC effects induced by electric fields of intensities $0 < \mathcal{E} < 4$ MV/cm (Fig.6b). The MD simulations involved the use of large supercells containing 96,000 atoms, Nosé-Hoover thermostats, Parrinello-Rahman barostats, and simulation times longer than 2 ns [28].

Field-induced MA dipole alignment has been observed in Liu and Cohen’s room-temperature MD simulations as shown by the shift in the peak of the probability distribution function estimated for the molecular dipoles calculated along the three Cartesian directions, $\{\mu_i\}_{x,y,z}$ (Fig.6c). However, it has been found that even under relatively high electric fields of the order of $|\mathcal{E}| \sim 1$ MV/cm

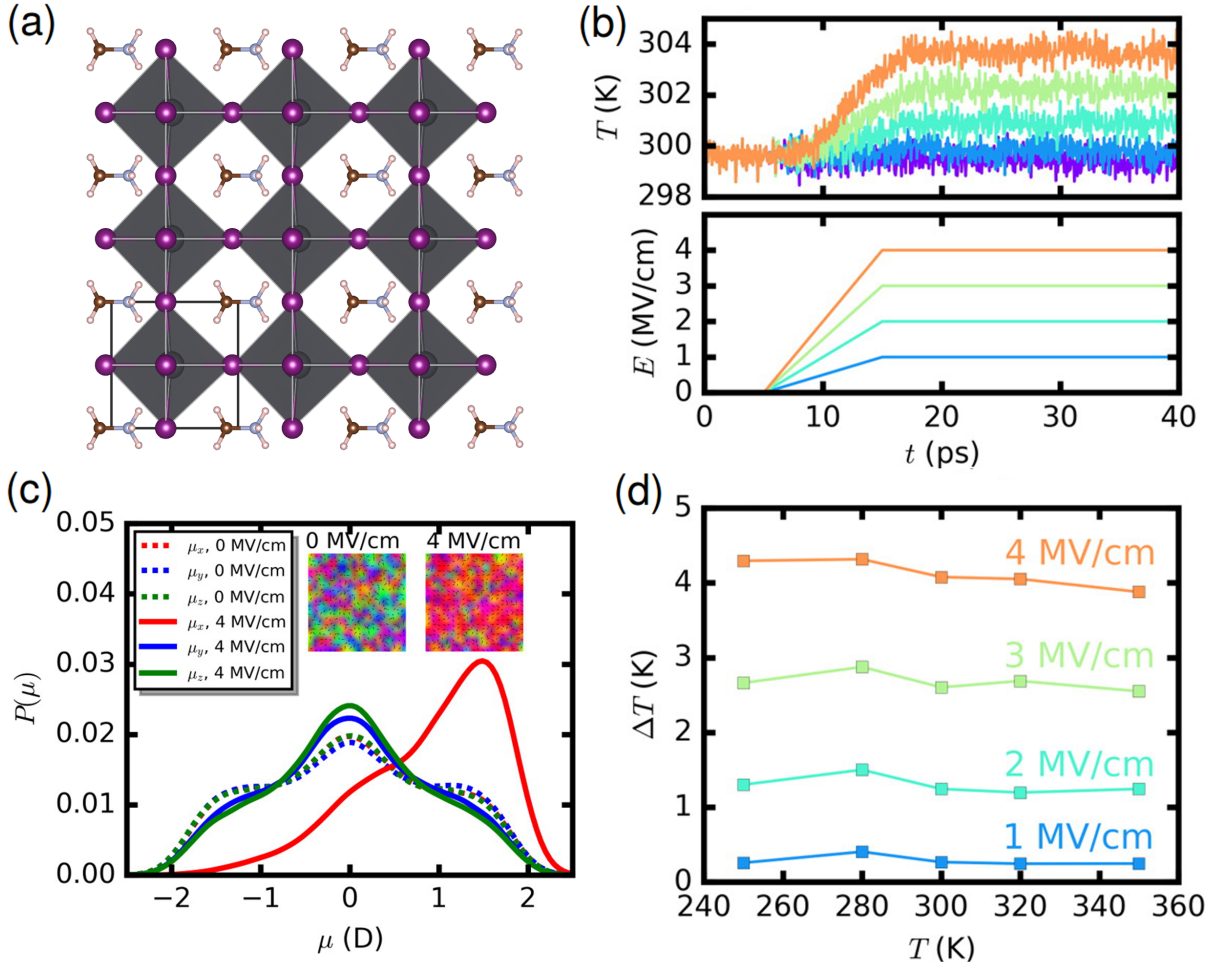


FIG. 6: Electrocaloric effects in the hybrid perovskite $\text{CH}_3\text{NH}_3\text{PbI}_3$ predicted with molecular dynamics simulations and the direct method. (a) Sketch of the atomic structure of MAPbI_3 . C, H, N, Pb, and I atoms are represented with brown, pink, violet, blue, and purple spheres, respectively. (b) Adiabatic thermal change of MAPbI_3 in response to electric fields of different intensity. (c) Probability distribution functions of the molecular CH_3NH_3 dipoles under several electric fields. The insets show the orientations of the molecular dipoles obtained from molecular dynamics simulations performed at 300 K. (d) Temperature and electric field dependence of the electrocaloric effect in MAPbI_3 . Reproduced from work [28].

the MA cations still can rotate, thus the resulting electric polarization is still quite small (i.e., $P \sim 0.01 \text{ C/m}^2$ [105]). This behaviour is in sharp contrast to what is observed for archetypal ferroelectrics like BaTiO_3 and PbTiO_3 where much larger electric dipole moments are achieved upon application of much smaller electric bias (i.e., $P \sim 0.1 \text{ C/m}^2$ [81]).

The adiabatic temperature changes predicted for MAPbI_3 at ambient conditions amount to 0.3 K for an electric field of 1 MV/cm and to 4.1 K for $\mathcal{E} = 4 \text{ MV/cm}$ (Fig.6d) [28]. The value of these external electric fields are quite high and thus likely to cause leakage current issues in practice due to the small band gap of MAPbI_3 . In addition, the estimated adiabatic temperature shifts are quite modest in comparison to those observed in ferroelectric oxide perovskites, which may oscillate from few

degrees up to 20 K [16]. Nevertheless, the temperature dependence of the calculated ΔT around $T = 300 \text{ K}$ is very weak (Fig.6d), which may be favorable for minimizing practical hysteresis and irreversibility problems [9, 103, and 104]. Such a ΔT temperature behaviour typically is found in relaxor ferroelectrics (see next subsection), which hints at the structural similarities between MAPbI_3 and other materials that exhibit polar domains at the nanoscale and low temperatures [106].

Liu and Cohen also have explored the combined action of epitaxial strain and electric fields on the polar and electrocaloric properties of MAPbI_3 at room temperature. In fact, the application of mechanical stresses offers very promising avenues in the field of caloric materials and solid-state cooling [107–109]. It has been found that under a small compressive biaxial strain of 2% a more com-

plete alignment of the MA cations can be achieved for an electric bias of 1 MV/cm (namely, a two-fold enhancement in comparison to the unstrained case [28]). Likewise, a significant increase on the electrocaloric response of MAPbI₃ has been demonstrated: for a compressive epitaxial strain of 4% the estimated ΔT 's are about two or three times larger than those calculated for the analogous free-standing system (e.g., 5.2 K for $\mathcal{E} = 2$ MV/cm [28]). These MD results, although may seem not relevant from an applied point of view, illustrate very well the capabilities of atomistic simulations for analyzing and predicting complex dynamical effects that can lead to original thermal behaviour in functional materials.

C. Relaxor ferroelectric BaZr_{1-x}Ti_xO₃

Relaxor ferroelectrics are a class of ferroelectric materials that present a dielectric response that is frequency-dependent and broad in temperature while remain macroscopically paraelectric down to absolute zero temperature [110–112]. Relaxor ferroelectrics typically exhibit high dielectric constants and also large electrostriction [113]. The microscopic origins of these phenomena are thought to be related to the existence of polar nanoregions below a particular temperature called the Burns temperature [114]. Examples of archetypal relaxor ferroelectrics are lead magnesium niobate (Pb₃MgNb₂O₉ – PMN–), lead scandium niobate (PbSc_{1-x}Nb_xO₃ – PSN–) and solid solutions like barium titanate-bismuth zinc niobium tantalate (BT-BZNT) and barium titanate-barium strontium titanate (BT-BST) [115–117].

Relaxor ferroelectrics appear to be also promising electrocaloric materials in which original thermal behaviour is driven by electric fields. For example, relatively large ΔT 's of 2–3 K have been measured directly in PMN-based oxides under small electric fields of 90 kV/cm [110]. The magnitude of the $\Delta T/\mathcal{E}$ coefficient is largest at the critical point in which the paraelectric to ferroelectric phase transition changes from first-order type to second-order type. Another illustrative example is provided by the lead-free relaxor ferroelectric Ba(Zr_{0.8}Ti_{0.2})O₃ in which a large adiabatic temperature change of ~ 5 K has been measured over a broad temperature interval of 30 K [118].

Jiang *et al.* have used a first-principles based effective Hamiltonian along with classical molecular dynamics and Monte Carlo simulations to investigate the electrocaloric response of the relaxor ferroelectric Ba(Zr_{0.5}Ti_{0.5})O₃ (BZT) in the temperature interval $100 \leq T \leq 500$ K (Fig.7) [29]. The employed BZT effective Hamiltonian has been shown to reproduce successfully the characteristic temperatures measured in experiments as well as the existence and the dynamics of polar nanoregions [119]. Jiang *et al.*'s simulations involve very large simulation cells containing $\sim 10,000$ atoms and the use of the indirect and direct estimation techniques described in Secs.III and V.

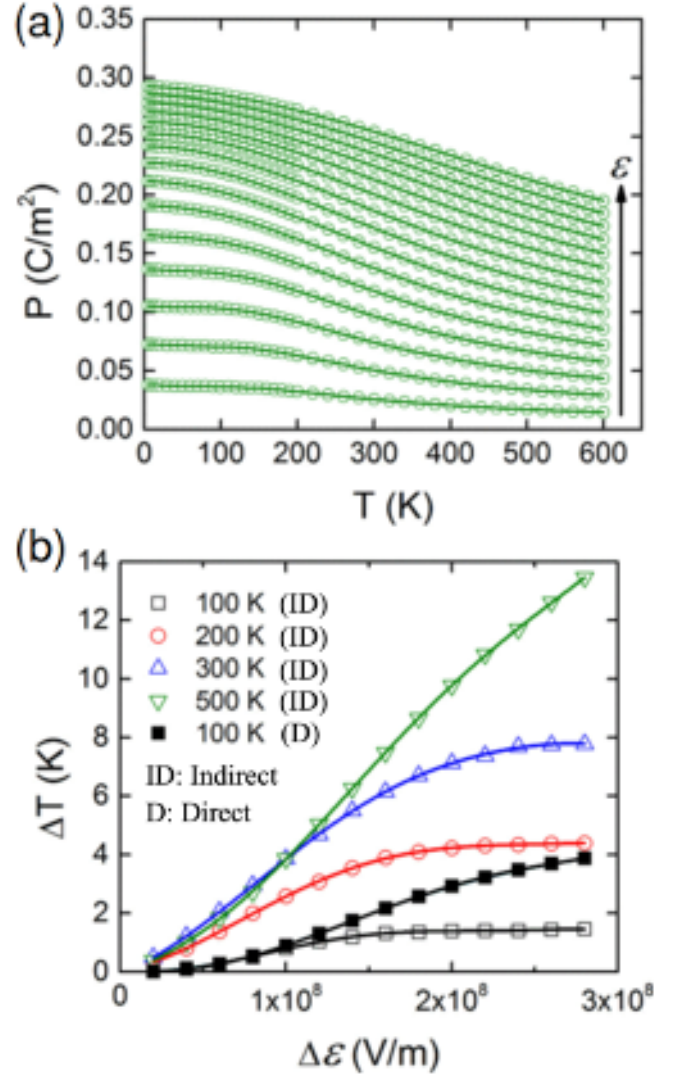


FIG. 7: Ferroelectric and electrocaloric properties estimated for the relaxor BaZr_{1-x}Ti_xO₃ by using an effective Hamiltonian model and molecular dynamics (direct method) and Monte Carlo simulations (indirect method). (a) Temperature dependence of the polarization under different electric bias. The electric field is applied on a fixed direction and its module changes from $2 \cdot 10^7$ to $3 \cdot 10^8$ V/m in increments of $2 \cdot 10^7$ V/m. (b) The adiabatic temperature change associated with the electrocaloric effect expressed as a function of temperature and maximum electric field. Reproduced from work [29].

Figure 7 shows the estimated variation of the electric polarization in the BZT relaxor as a function of temperature and electric field module along with the corresponding electrocaloric adiabatic temperature changes. Relatively large ΔT of about 8 K are predicted near room temperature for moderately large electric fields of the order of ~ 1 MV/cm. The temperature and electric field dependences of the estimated adiabatic temperature in-

tervals are not monotonous, as it is expected from relaxor ferroelectrics [117]. In particular, small values of the adiabatic electrocaloric coefficient, defined as $(\partial T/\partial \mathcal{E})_S$, are obtained at low \mathcal{E} 's, followed by a sustained increase up to a maximum value beyond which it decreases for larger electric fields.

Interestingly, Jiang *et al.* have found that indirect and direct estimations of the electrocaloric effect in BZT do not coincide at temperatures below the corresponding Burns point (Fig.7b) when polar nanoregions emerge [29]. The reasons for such numerical inconsistencies are related to the occurrence of non-ergodic processes at low temperatures. In this case, direct estimation techniques can reproduce non-equilibrium phenomena with certain reliability and thus are the methods of choice for simulating caloric effects in relaxor ferroelectrics. Actually, a similar failure of indirect methods caused by nonergodicity has been demonstrated experimentally for the ferroelectric relaxor polymer poly(vinylidene fluoride-trifluoroethylene-chlorofluoroethylene) [P(VDF-TrFE-CFE)] [120]. The present study illustrates once again the capabilities of first-principles based methods for simulating complex atomistic behaviour in promising materials that render sizable electrocaloric effects.

VII. CONCLUSIONS

First-principles based computational techniques for simulation of electrocaloric effects in oxide perovskites and similar polar materials are already mature and well established. These simulation methods (e.g., quasi-harmonic free-energy methods and effective Hamiltonians) were originally developed for the study of temperature and field-induced phase transformation in materials and have already demonstrated great success in other research disciplines.

The suite of computational approaches reviewed in this Chapter can be used to reproduce with reliability the electrocaloric performance of complex materials like multiferroics, in which the electronic and lattice degrees of freedom are strongly coupled, organic-inorganic halide perovskites, in which the molecular cations can be orientationally disordered, and ferroelectric relaxors, in which the existence of polar nanoregions and non-ergodic processes underpin their physical behaviour. Analogous electrocaloric simulation success can be achieved for other functional materials that exhibit complex and unconventional responses to electric fields.

First-principles based simulation of electrocaloric effects, therefore, can help enormously in developing new materials and strategies for boosting solid-state cooling engineered on electric fields. Thus, the current pressing challenge of finding new refrigeration technologies that are environmentally friendly and highly scalable in size can benefit vastly from the outcomes of such accurate and reliable simulation methods.

-
- [1] Zhong, W., King-Smith, R. D. & Vanderbilt, D. Phys. Rev. Lett. **72**, 3618 (1994).
 - [2] Cazorla, C. & Íñiguez, J. Phys. Rev. B **88**, 214430 (2013).
 - [3] Cazorla, C., Diéguez, O. & Íñiguez, J. Sci. Adv. **3**, e1700288 (2017).
 - [4] Heo, Y., Hu, S., Sharma, P., Kim, K.-E., Jang, B.-K., Cazorla, C., Yang, C.-H. & Seidel, J. ACS Nano **11**, 2805 (2017).
 - [5] Spaldin, N. A. & Ramesh, R. Nat. Mater. **18**, 203 (2019).
 - [6] Grinberg, I., West, D. V., Torres, M., Gou, G., Stein, D. M., Wu, L., Chen, G., Gallo, E. M., Akbashev, A. R., Davies, P. K., Spanier, J. E. & Rappe, A. M. Nature **503**, 509 (2013).
 - [7] Cazorla, C., Ganduglia-Pirovano, M. V. & Carrasco, J. Front. Chem. **7**, 547 (2019).
 - [8] Narvaez, J., Vasquez-Sancho, F. & Catalan, G. Nature **538**, 219 (2016).
 - [9] Cazorla, C. Appl. Phys. Rev. **6**, 041316 (2019).
 - [10] Moya, X., Kar-Narayan, S. & Mathur, N. D. Nat. Mater. **13**, 439 (2014).
 - [11] Aznar, A., Lloveras, P., Romanini, M., Barrio, M., Tamarit, J. Ll., Cazorla, C., Errandonea, D., Mathur, N. D., Planes, A., Moya, X. & Mañosa, Ll. Nat. Commun. **8**, 1851 (2017).
 - [12] Cazorla, C. & Errandonea, D. Nano Lett. **16**, 3124 (2016).
 - [13] Scott, J. F. Annu. Rev. Mater. Res. **41**, 229 (2011).
 - [14] Pecharsky, V. K. & Gschneidner, Jr. K. A. Phys. Rev. Lett. **78**, 4494 (1997).
 - [15] Bonnot, E., Romero, R., Mañosa, Ll., Vives, E. & Planes, A. Phys. Rev. Lett. **100**, 125901 (2008).
 - [16] Shirsath, S. E. *et al.* Nano Letters **20**, 1262 (2020).
 - [17] Lisenkov, S. & Ponomareva, I. Phys. Rev. B **80**, 140102 (2009).
 - [18] Wang, H. *et al.* Scr. Mater. **178**, 150 (2020)
 - [19] Herchig, R., Chang, C.-M., Mani, B.-K. & Ponomareva, I. Sci. Rep. **5**, 17294 (2015).
 - [20] Cazorla, C. Res. Phys. **5**, 262 (2015).
 - [21] Kresse, G. & Furthmüller, J. Phys. Rev. B **54**, 11169 (1996).
 - [22] Togo, A. & Tanaka, I. Scr. Mater. **108**, 1 (2015).
 - [23] Gale, J. D. J. Chem. Soc. Faraday Trans. **93**, 629 (1997).
 - [24] Plimpton, S. J. Comp. Phys. **117**, 1 (1995).
 - [25] Paul, J., Nishimatsu, T., Kawazoe, Y. & Waghmare, U. V. Appl. Phys. Lett. **93**, 242905 (2008).
 - [26] Wojdel, J. C., Hermet, P., Ljungberg, M. P., Ghosez, Ph. & Íñiguez, J. J. Phys.: Condens. Matt. **25**, 305401 (2013); Escorihuela-Sayalero, C., Wojdel, J. C. &

- Íñiguez, J. Phys. Rev. B **95**, 094115 (2017).
- [27] Cazorla, C. & Íñiguez, J. Phys. Rev. B **98**, 174105 (2018).
- [28] Liu, S. & Cohen, R. E. J. Phys. Chem. C **120**, 17274 (2016).
- [29] Jiang, Z., Prokhorenko, S., Prosandeev, S., Nahas, Y., Wang, D., Íñiguez, J., Defay, E. & Bellaiche, L. Phys. Rev. B **96**, 014114 (2017).
- [30] Kohn, W. & Sham, L. J. Phys. Rev. **140**, A1133 (1965).
- [31] Sham, L. J. & Kohn, W. Phys. Rev. **145**, 561 (1966).
- [32] Langreth, D. C. & Perdew, J. P. Solid State Commun. **17**, 1425 (1975).
- [33] Nguyen, H.-V. & de Gironcoli, S. Phys. Rev. B **79**, 205114 (2009).
- [34] Ceperley, D. M. & Alder, B. J. Phys. Rev. Lett. **45**, 566 (1980).
- [35] Perdew, J. P. & Zunger, A. Phys. Rev. B **23**, 5048 (1981).
- [36] Perdew, J. P., J. A. Chevary, S. H. Vosko, K. A. Jackson, M. R. Pederson, D. J. Singh & Fiolhais, C. Phys. Rev. B **46**, 6671 (1992).
- [37] Perdew, J. P., K. Burke & Ernzerhof, M. Phys. Rev. Lett. **77**, 3865 (1996).
- [38] Sun, J., Ruzsinszky, A. & Perdew, J. P. Phys. Rev. Lett. **115**, 036402 (2015).
- [39] Zhang, Y. *et al.* npj Comp. Mater. **4**, 9 (2018).
- [40] Becke, A. D. J. Chem. Phys. **98**, 5648 (1993).
- [41] Adamo, C. & Barone, V. J. Chem. Phys. **110**, 6158 (1999).
- [42] Krukau, A. V., Vydrov, O. A., Izmaylov, A. F. & Scuseria, G. E. J. Chem. Phys. **125**, 224106 (2006).
- [43] Franchini, C. J. Phys. Condens. Matt. **26**, 253202 (2014).
- [44] Bilc, D. I., Orlando, R., Shaltaf, R., Rignanese, G.-M., Íñiguez, J. & Ghosez, Ph. Phys. Rev. B **77**, 165107 (2008).
- [45] Evarestov, R. A. & Bandura, A. V. J. Comp. Chem. **33**, 1123 (2012).
- [46] Rivero, P. & Cazorla, C. Phys. Chem. Chem. Phys. **18**, 30686 (2016).
- [47] Cazorla, C. Phys. Rev. Appl. **7**, 044025 (2017).
- [48] Ercolessi, F. & Adams, J. B. Europhys. Lett. **26**, 583 (1994).
- [49] Cazorla, C. & Boronat, J. Phys. Rev. B **92**, 224113 (2015).
- [50] Mattoni, A., Filipetti, A., Saba, M. I. & Delugas, P. J. Phys. Chem. C **119**, 17421 (2015).
- [51] Hata, T., Giorgi, G., Yamashita, K., Caddeo, C. & Mattoni, A. J. Phys. Chem. C **121**, 3724 (2017).
- [52] Cazorla, C., Sagotra, A. K., King, M. & Errandonea, D. J. Phys. Chem. C **122**, 1267 (2018).
- [53] Tinte, S., Stachiotti, M. G., Sepiarsky, M., Migoni, R. L. & Rodriguez, C. O. J. Phys.:Condens. Matt. **11**, 9679 (1999).
- [54] Jackson, R. A. & Valerio, M. E. G. J. Phys.:Condens. Matt. **17**, 837 (2005).
- [55] Sepiarsky, M., Phillpot, S. R., Wolf, D., Stachiotti, M. G. & Migoni, R. L. J. Appl. Phys. **90**, 4509 (2001).
- [56] Hashimoto, T. & Moriwake, H. Mol. Simul. **41**, 1074 (2015).
- [57] Gambuzzi, E. & Pedone, A. Phys. Chem. Chem. Phys. **16**, 21645 (2014).
- [58] Cohen, R. E. Nature **358**, 136 (1992).
- [59] Haomin, C. & Adams, S. IUCrJ **4**, 614 (2017).
- [60] Grinberg, I., Cooper, V. R. & Rappe, A. M. Nature **419**, 909 (2002).
- [61] Grinberg, I., Cooper, V. R. & Rappe, A. M. Phys. Rev. B **69**, 144118 (2004).
- [62] Shin, Y.-H., Cooper, V. R., Grinberg, I. & Rappe, A. M. Phys. Rev. B **71**, 054104 (2005).
- [63] Liu, S., Grinberg, I., Takenaka, H. & Rappe, A. M. Phys. Rev. B **88**, 104102 (2013).
- [64] Xu, R., Liu, S., Grinberg, I., Karthik, J., Damodaran, A. R., Rappe, A. M. & Martin, L. W. Nat. Mater. **14**, 79 (2015).
- [65] Qi, Y., Liu, S., Lindenberg, A. M. & Rappe, A. M. Phys. Rev. Lett. **120**, 055901 (2015).
- [66] Zhong, W. & Vanderbilt, D. Phys. Rev. B **52**, 6301 (1995).
- [67] Paul, A., Sun, J., Perdew, J. P. & Waghmare, U. V. Phys. Rev. B **95**, 054111 (2017).
- [68] Prosandeev, S., Wang, D., Akbarzadeh, A. R. & Bellaiche, L. J. Phys.:Condens. Matt. **27**, 223202 (2015).
- [69] Zubko, P., Wojdel, J. C., Hadjimichael, M., Fernandez-Pena, S., Sene, A., Lukyanchuk, I., Triscone, J.-M. & Íñiguez, J. Nature **534**, 524 (2016).
- [70] Frenkel, D. & Smit, B. *Understanding Molecular Simulation*. Academic Press, Inc., 6277 Sea Harbor Drive Orlando, FL., United States, ISBN:978-0-12-267351-1.
- [71] Metropolis, N., Rosenbluth, A. W., Rosenbluth, M. N., Teller, A. & Teller, E. J. Chem. Phys. **21**, 1087 (1953).
- [72] Marathe, M., Grünebohm, A., Nishimatsu, T., Entel, P. & Ederer, C. Phys. Rev. B **93**, 054110 (2016).
- [73] Jiang, Z., Nahas, Y., Prokhorenko, S., Prosandeev, S., Wang, D., Íñiguez, J., Defay, E. & Bellaiche, L. Phys. Rev. B **97**, 104110 (2018).
- [74] Cazorla, C. & Boronat, J. Rev. Mod. Phys. **89**, 035003 (2017).
- [75] Baroni, S., Giannozzi, P. & Isaev, E. Rev. Mineral. Geochem. **71**, 39 (2010).
- [76] Cazorla, C., Errandonea, D. & Sola, E. Phys. Rev. B **80**, 064105 (2009).
- [77] Lang, S. B. Phys. Today **58**, 31 (2005).
- [78] Liu, J. & Pantelides, S. T. Phys. Rev. Lett. **120**, 207602 (2018).
- [79] Liu, J., Fernández-Serra, M. V. & Allen, P. B. Phys. Rev. B **93**, 081205(R) (2017).
- [80] Born, M. Rev. Mod. Phys. **17**, 245 (1945).
- [81] Cazorla, C. & Stengel, M. Phys. Rev. B **92**, 214108 (2015).
- [82] Taioli, S., Cazorla, C., Gillan, M. J. & Alfè, D. Phys. Rev. B **75**, 214103 (2007).
- [83] Cazorla, C., Gillan, M. J., Taioli, S. & Alfè, D. J. Chem. Phys. **126**, 194502 (2007).
- [84] Cazorla, C., & Alfè, D. & Gillan, M. J. Phys. Rev. B **85**, 064113 (2012).
- [85] Tadano, T. & Tsuneyuki, S. Phys. Rev. B **92**, 054301 (2015).
- [86] Souvatzis, P., Eriksson, O., Katsnelson, M. I. & Rudin, S. P. Phys. Rev. Lett. **100**, 095901 (2008).
- [87] Souvatzis, P. J. Phys.:Condens. Matter **23**, 445401 (2011).
- [88] Chen, P., Grisolia, M. N., Zhao, H. J., Gonzalez-Vzquez, O. E., Bellaiche, L., Bibes, M., Liu, B.-G. & Íñiguez, J. Phys. Rev. B **97**, 024113 (2018).
- [89] Azuma, M., Niitaka, S., Hayashi, N., Oka, K., Takano,

- M., Funakubo, H. & Shimakawa, Y. *Jpn. J. Appl. Phys.* **47**, 7579 (2008).
- [90] Hojo, H., Oka, K., Shimizu, K., Yamamoto, H., Kawabe, R. & Azuma, M. *Adv. Mater.* **30**, 1705665 (2018).
- [91] Yang, W. *et al. Science* **356**, 1376 (2017).
- [92] Tan, Z. *et al. Nat. Nanotechnol.* **9**, 687 (2014).
- [93] Ren, L. *et al. J. Phys. Chem. Lett.* **11**, 2577 (2020).
- [94] Ye, H.-Y. *et al. Science* **361**, 151 (2018).
- [95] Horiuchi, S. & Tokura, Y. *Nat. Mater.* **7**, 357 (2008).
- [96] Rakita, Y., Bar-Elli, O., Meirzadeh, E., Kaslasi, H., Peleg, Y., Hodes, G., Lubomirsky, I., Oron, D., Ehre, D. & Cahen, D. *Proc. Natl. Acad. Sci.* **114**, E5504 (2017).
- [97] Hoque, M. N. F., Yang, M., Li, Z., Islam, N., Pan, X., Zhu, K. & Fan, Z. *ACS Energy Lett.* **1**, 142 (2016).
- [98] Weller, M. T., Weber, O. J., Henry, P. F., Di Pumpo, A. M. & Hansen, T. C. *Chem. Commun.* **51**, 4180 (2015).
- [99] Mosconi, E., Quarti, C., Ivanovska, T., Ruani, G. & De Angelis, F. *Phys. Chem. Chem. Phys.* **16**, 16137 (2014).
- [100] Carignano, M. A., Kachmar, A. & Hutter, J. *J. Phys. Chem. C* **119**, 8991 (2015).
- [101] Cazorla, C. *Nature* **567**, 470 (2019).
- [102] Li, B. *et al. Nature* **567**, 506 (2019).
- [103] Lloveras, P. *et al. Nat. Commun.* **10**, 1803 (2019).
- [104] Aznar, A. *et al. J. Mater. Chem. A* **8**, 639 (2020).
- [105] Stroppa, A., Quarti, C., De Angelis, F. & Picozzi, S. *J. Phys. Chem. Lett.* **6**, 2223 (2015).
- [106] Acosta, M. *et al. Sci. Rep.* **6**, 28742 (2016).
- [107] Sagotra, A. K., Errandonea, D. & Cazorla, C. *Nat. Commun.* **8**, 963 (2017).
- [108] Sagotra, A. K., Chu, D. & Cazorla, C. *Nat. Commun.* **9**, 3337 (2018).
- [109] Min, J., Sagotra, A. K. & Cazorla, C. *Phys. Rev. Mater.* **4**, 015403 (2020).
- [110] Rozic, B., Kosec, M., Ursic, H., Holc, J., Malic, B., Zhang, Q. M., Blinc, R., Pirc, R. & Kutnjak, Z. *J. Appl. Phys.* **110**, 064118 (2011).
- [111] Pirc, R., Kutnjak, Z., Blinc, R. & Zhang, Q. M. *J. Appl. Phys.* **110**, 074113 (2011).
- [112] Bokov, A. A. & Ye, Z.-G. *J. Adv. Dielectr.* **2**, 1241010 (2012).
- [113] Cross, L. E., Jang, S. J., Newnham, R. E., Nomura, S. & Uchino, K. *Ferroelectrics* **23**, 187 (1980).
- [114] Bokov, A. A. & Ye, Z.-G. *J. Mater. Sci.* **41**, 31 (2006).
- [115] Kong, S., Kumar, N., Checchia, S., Cazorla, C. & Daniels, J. *Adv. Funct. Mater.* **29**, 1900344 (2019).
- [116] Mohanty, H. *et al. J. Phys.: Condens. Matt.* **31**, 075401 (2019).
- [117] Zhou, Y., Lin, Q., Liu, W. & Wang, D. *RSC Adv.* **6**, 14084 (2016).
- [118] Qian, X.-S., Ye, H.-J., Zhang, Y.-T., Gu, H., Li, X., Randall, C. A. & Zhang, Q. M. *Adv. Funct. Mater.* **24**, 1300 (2014).
- [119] Akbarzadeh, A. R., Prosandeev, S., Walter, E. J., Al-Barakaty, A. & Bellaiche, L. *Phys. Rev. Lett.* **108**, 257601 (2012).
- [120] Lu, S. G. *et al. Appl. Phys. Lett.* **97**, 202901 (2010).